

# Real-time alignment and co-phasing of multi-aperture systems using phase diversity

Vievard S.<sup>a,b</sup>, Cassaing F.<sup>a</sup>, Bonnefois A.<sup>a</sup>, Mugnier L. M.<sup>a</sup>, and Montri J.<sup>a</sup>

<sup>a</sup>ONERA, The French Aerospace Lab, F-92240, Chatillon, France

<sup>b</sup>Thales Alenia Space, 5 Allée des Gabians, 06150 Cannes, France

## ABSTRACT

The alignment of the subapertures is a major challenge for future segmented telescopes and telescope arrays. We show here that a phase diversity sensor using two near-focus images can fully and efficiently align a multiple aperture system, both for the alignment (large amplitude tip/tilt aberrations correction) and phasing (piston and small amplitude tip/tilt aberrations correction) modes. We derive a new algorithm for the alignment of the subapertures : ELASTIC. We quantify the novel algorithm performance by numerical simulations and we demonstrate it experimentally on a test bench. We also study the performance of LAPD, a recent real-time algorithm for the phasing of the sub-apertures. This work should simplify the design of future multiple aperture systems.

**Keywords:** Multi-aperture systems, Phase diversity, Phasing system, Segmented mirror, Wavefront sensing

## 1. CONTEXT AND MOTIVATION

The resolution of a telescope is ultimately limited by its aperture diameter. The latter is limited by current technology to about 10 meters for ground-based telescopes and a few meters for space-based telescopes because of volume and mass considerations. Multi-aperture telescopes (interferometers) have the potential to remove these limitations. Space segmented telescope projects aim at astronomical (the JWST, TALC,<sup>1</sup> WFIRST-AFTA<sup>2</sup>) or Earth (HOASIS<sup>3</sup>) observations. Ground-based segmented telescopes already exist (Kecks) or are planned in a close future (E-ELT, TMT).

In order to reach the diffraction limit, a precise control of the sub-apertures is necessary. This so-called control consists in the measurement and correction of misalignments between sub-apertures, which are the specific aberrations of interferometry and can be described on each sub-aperture by the first three Zernike polynomials, called piston and tip-tilt. The alignment of the sub-apertures from a possible large-amplitude perturbation case (defined as follow as the coarse alignment mode) up to a fine small-amplitude perturbation case (defined as follow as the phasing mode) is a difficult task. Phase measurements are indeed difficult with quadratic optical detectors.

Focal-plane wavefront sensing is an elegant solution to measure the misalignments. Since the focal (and near-focal) image(s) of any source taken by a 2D camera shows distortions when the system is not perfectly aligned, the system misalignments can be retrieved by solving the associated problem. The main interest of this technique is that this wavefront sensor is included in the main imaging detector, simplifying the hardware and minimizing differential paths. The phase retrieval technique, based on the sole focal-plane image, is generally not sufficient to retrieve piston and tip/tilt without ambiguity except in specific cases.<sup>4</sup> The phase diversity technique<sup>56</sup>, typically based on a focal and a slightly defocused images, removes all ambiguities and operate even on unknown extended sources. Usually used for small-amplitude errors, the associated algorithms are iterative and consequently time-consuming.

The aim of this paper is to present a method to efficiently align a multi-aperture telescope with low computing cost. First, we present in section 2 a new method for large amplitude errors estimation based on the sole use of two images, quite similar to the Phase Diversity technique : ELASTIC (Estimation of Large Amplitude Subaperture

---

Further author information: (Send correspondence to Sebastien VIEVARD)

S. Vievard: E-mail: sebastien.vievard@onera.fr, Telephone: +33 (0)1 46 73 49 23

Tip-tilt by Image Correlation) algorithm. We describe this algorithm, quantify its performance by numerical simulations and experimentally demonstrate its capability. Then, in section 3, we study the performance of a recent analytical (and potentially real-time) estimator nicknamed LAPD for Linearized Algorithm using Phase Diversity<sup>7</sup>.

## 2. LARGE AMPLITUDE TIP/TILT ALIGNMENT WITH GEOMETRIC DIVERSITY

The first step to reach the diffraction limit for a multi-aperture instrument is the measurement and correction of large amplitude tip/tilt errors between the sub-apertures. The use of classical phase diversity algorithms is impossible in these conditions. Indeed, these algorithms require that the beams from the different sub-apertures already interfere in order to work, and in particular that they are superimposed. Future multi-aperture systems will face the alignment problem and will need an efficient method to measure and correct large amplitude errors at a low computing cost.

In the context of JWST large amplitude alignment, Thurman proposed a geometric technique<sup>8</sup> permitting to extend the normal phase retrieval capture range. This method, refined by Alden,<sup>9</sup> provides an estimation of the error thanks to intensity measurements in multiple planes up to the focal plane. This estimation is then used as a starting guess. Series of defocused images will be acquired thanks to a lens wheel, and will be sent to Earth for estimation feedback. This should be iteratively processed until the complete phasing, and should take nearly a week of commissioning time.<sup>10</sup>

We propose in this section a new geometric diversity technique that can provide a simple and non-supervised estimation of full-field tip/tilt errors, using only two near-focus planes, so that the correction can be performed in full autonomy by the instrument itself in a closed-loop sequence with a limited hardware.

### 2.1 Optical Transfer Function (OTF) of a multi-aperture instrument in alignment mode

As it will be used in the next section to detail the algorithm, we derive here the OTF of a strongly misaligned multi-aperture instrument. We assume that sub-apertures have the same shape and the complex transmission  $\mathbf{p}_n$  :

$$\mathbf{p}_n(\mathbf{u}) = \left[ \Pi(\mathbf{u}) \exp \left[ j \sum_{k=1}^{k_{max}} a_{kn} \mathbf{Z}_k(\mathbf{u}) \right] \right] \star \delta(\mathbf{u} - \mathbf{u}_n) \quad (1)$$

where  $\mathbf{u}_n$  is the center of the  $n^{\text{th}}$  subaperture and the modulus is described by the disk function  $\Pi$ ,

$$\Pi(\mathbf{u}) = \begin{cases} 1 & \text{for } 0 \leq |\mathbf{u}| \leq R \quad \text{with } R \text{ the pupil radius} \\ 0 & \text{elsewhere} \end{cases}$$

In Eq.(1), the phase of  $\mathbf{p}_n$  is expanded on  $k_{max}$  scaled Zernike polynomials  $\mathbf{Z}_k$ .  $a_{kn}$  is the rms amplitude of the  $k^{\text{th}}$  mode over the  $n^{\text{th}}$  sub-aperture and  $j^2 = -1$ . Note that in our case,  $k_{max} = 3$  (1: piston, 2-3: tip-tilt).

The OTF of a  $N$ -aperture instrument (with for example 3 apertures, cf Fig.1a), defined as the pupil auto-correlation, is the sum of  $N^2$  peaks :  $N$  superimposed photometric peaks (central peak of the OTF, cf Fig.1b) and  $N(N - 1)$  interferometric peaks (peaks around the central peak, cf Fig.1b).

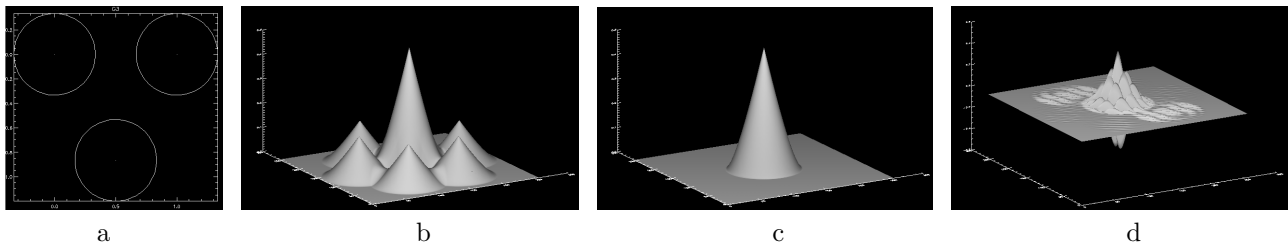


Figure 1. a. Goly 3 pupil configuration ; b. Goly 3 coherent OTF (aligned) ; c. Goly 3 incoherent OTF (aligned) ; d. Goly 3 coherent OTF (large differential tip/tilts between sub-apertures).

In the alignment case, the interferometric peaks can be neglected because of the large amplitude tip/tilt errors (cf the difference between Fig.1b and d) and the *a priori* large piston error with respect to the coherence length, which puts the instrument in an incoherent mode (cf Fig.1c-). The information we are looking for has thus to be found in the central photometric peaks (cf the large sinusoidal modulation in Fig.1d). The algorithm proposed in next section relies only on those photometric peaks. If necessary, interferometric peaks can also be removed with a low-pass filter. It comes that the OTF of a  $N$ -aperture misaligned instrument can be written as the sum of the OTFs of each sub-aperture:

$$OTF(\mathbf{u}) = \sum_{n=1}^N (\mathbf{p}_n \star \mathbf{p}_n)(\mathbf{u}) \quad (2)$$

The autocorrelation of the pupil "kills" the piston information introduced in the pupil, but retains the tip/tilt information. We then have :

$$OTF(\mathbf{u}) = \sum_{n=1}^N \Lambda_n(\mathbf{u}) \exp \left[ j \sum_{k=2}^3 a_{kn} \mathbf{Z}_k(\mathbf{u}) \right] \quad (3)$$

with  $\Lambda_n(\mathbf{u}) = (\mathbf{p}_n \star \mathbf{p}_n)(\mathbf{u})$  and  $a_{kn}$  the aberration coefficient we want to estimate.

## 2.2 Principle of the algorithm

The information we want to obtain are the  $a_{kn}$  coefficients in Eq.(3). The key to retrieve this information is to compute the intercorrelation between the focal and the defocused images. This correlation is easier to compute in the Fourier domain where it results in a simple termwise multiplication of the OTFs. In addition, we conjugate and shift one OTF along one direction ( $u_x$  or  $u_y$ ) by  $\Delta$  pixels. Because our study is limited to the point source observation of the instrument, we name  $OTF$  the Fourier Transform of the images (PSFs : Point Spread Functions). Therefore, we compute  $T = OTF^f * \overline{OTF^d}^{\Delta}$  where  $OTF^f$  is the focal image Fourier Transform and  $\overline{OTF^d}^{\Delta}$  is the shifted conjugated Fourier Transform of the defocused image :

$$T(\mathbf{u}) = \sum_{n=1}^N \Lambda_n^f(\mathbf{u}) \exp \left[ j \sum_{k=2}^3 a_{kn} \mathbf{Z}_k(\mathbf{u}) \right] \sum_{n'=1}^N \Lambda_{n'}^d(\mathbf{u} + \Delta \mathbf{u}) \exp \left[ -j \sum_{k'=2}^3 a_{k'n'} \mathbf{Z}_{k'}(\mathbf{u} + \Delta \mathbf{u}) \right] \quad (4)$$

With  $C_{n,n'}$  the multiplication of both OTF (in the focal plane,  $\Lambda_n^f(\mathbf{u})$ , and in the defocused plane,  $\Lambda_{n'}^d(\mathbf{u} + \Delta \mathbf{u})$ ), and because the  $Z_2$  and  $Z_3$  polynomials are linear, we can develop :

$$T(\mathbf{u}) = \sum_{n=1}^N \sum_{n'=1}^N C_{n,n'}(\mathbf{u}) \exp \left[ j \sum_{k=2}^3 a_{kn} \mathbf{Z}_k(\mathbf{u}) \right] \exp \left[ -j \sum_{k'=2}^3 a_{k'n'} (\mathbf{Z}_{k'}(\mathbf{u}) + \mathbf{Z}_{k'}(\Delta \mathbf{u})) \right] \quad (5)$$

$$T(\mathbf{u}) = \underbrace{\sum_{n=1}^N C_{n,n}(\mathbf{u}) \exp \left[ -j \sum_{k=2}^3 a_{kn} \mathbf{Z}_k(\Delta \mathbf{u}) \right]}_{\text{Auto-term}} + \underbrace{\sum_{n \neq n'}^N C_{n,n'}(\mathbf{u}) \exp \left[ -j \sum_{k=2}^3 (a_{kn} - a_{k'n'}) \mathbf{Z}_k(\mathbf{u}) + a_{k'n'} \mathbf{Z}_k(\Delta \mathbf{u}) \right]}_{\text{Inter-term}} \quad (6)$$

Eq.(6) shows that we have two terms : the "auto-terms" and the "inter-terms". The "auto-terms" are the correlation between the OTF of the  $n^{\text{th}}$  pupil in the focal plane with the shifted conjugated OTF of the same  $n^{\text{th}}$  pupil in the defocused plane. The "inter-terms" are the correlation between the OTF of each pupil in the focal plane, with the shifted conjugated OTF of each other pupil in the defocused plane. Eq.(6) also shows the interest of the shift : the tip/tilt information that would have disappear without shifting the conjugated OTF is converted into a piston. Indeed with  $k = 2$  or  $3$ ,  $Z_k(\Delta \mathbf{u})$  is a constant depending on the direction and the amplitude of the pixel shift. This piston is alone on the auto-terms, and is added to the tip/tilt in the inter-terms.

To illustrate this, we simulate the focal and the defocused images of an unresolved object with a strongly misaligned 7 sub-aperture instrument (Fig.2a and b). The effect of the defocus on the images can be seen on Fig.2b. For convenience, we show the correlation of the focal image with itself (Fig.2c), and the correlation of the focal image with the defocused image (Fig.2d). In the two cases, we can see the "auto-terms" in the circle, and the "inter-terms" all around. We see that all the "auto-terms" are superimposed in the case of the correlation between the focal plane and itself : we cannot extract any information from these "auto-terms". However, we see that the "auto-terms" of the focal plane and defocused plane correlation are separated. The defocus helps us to separate each sub-aperture information. The "auto-terms" positions are determined by the introduced defocus and the "inter-term" positions depend on the image spots separation : when the amplitude error is large (in our case), the "inter-terms" are well separated from the "auto-terms" (as we can see Fig.2d).

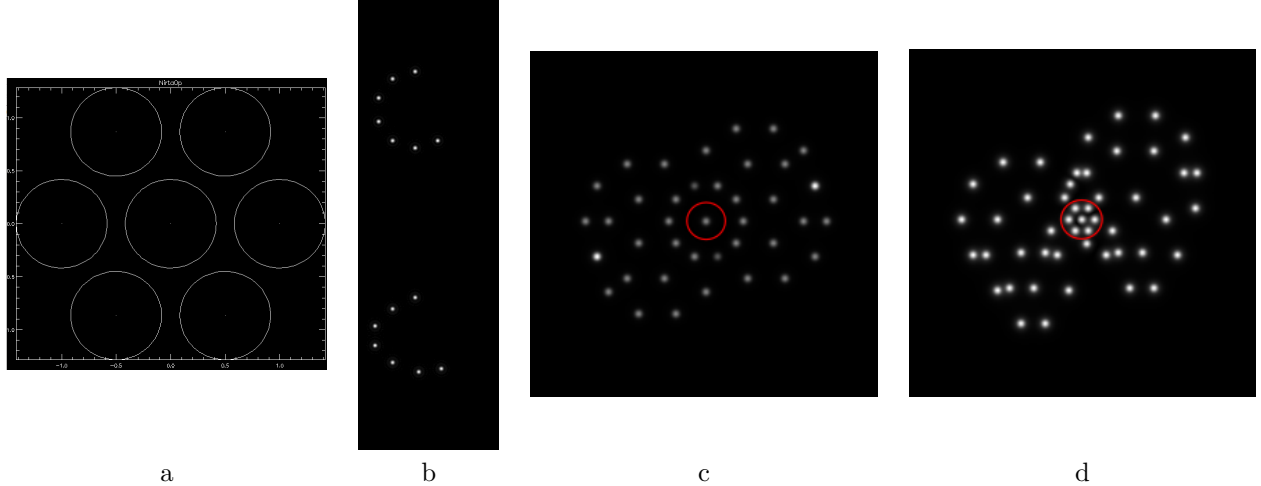


Figure 2. a. 7 sub-aperture configuration ; b. Focal (up) and 5 rad RMS defocused (down) images of an unresolved object from the misaligned instrument. Each spot is the image (PSF) of one subaperture ; c. Correlation of the focal image with itself (auto-terms of the correlation in the red circle) ; d. Correlation of the focal image and the defocused image (auto-terms of the correlation in the red circle)

Assuming that the sub-aperture PSFs are sufficiently separated, the "inter-terms" outside the circle can be filtered and Eq.(6) then becomes, with  $n = n'$  :

$$T(\mathbf{u}) = \sum_n C_{n,n}(\mathbf{u}) \exp \left[ -j \sum_{k=2}^3 a_{kn} \mathbf{Z}_k(\Delta \mathbf{u}) \right] \quad (7)$$

For each direction ( $u_x$  or  $u_y$ ) corresponding to tip or tilt search, we can write Eq.(7) as :

$$\begin{cases} \mathbf{T}_x = \mathbf{C}_x \gamma_x & \text{for the tip search, with a shift along } u_x \\ \mathbf{T}_y = \mathbf{C}_y \gamma_y & \text{for the tilt search, with a shift along } u_y \end{cases} \quad (8)$$

With  $\mathbf{T}_x$  and  $\mathbf{T}_y$  the images correlation values with a shift along one direction and the other,  $\mathbf{C}_x$  and  $\mathbf{C}_y$  the pupil's reference modes (with a shift along one direction and the other) without aberration and  $\gamma_x$  and  $\gamma_y$  the aberrations amplitudes. Since Eq.(8) are linear systems, they can easily be inverted (in a least-square sense since they are *a priori* rectangular). In this goal, we compute the Singular Value Decomposition (SVD) of (for example)  $\mathbf{C}_x$  :

$$\mathbf{C}_x = \mathbf{U}_x \mathbf{\Delta}_x \mathbf{V}_x^H \quad (9)$$

where  $\mathbf{U}_x$  and  $\mathbf{V}_x^H$  are regular change-of-basis matrices and  $\mathbf{\Delta}_x$  a diagonal decreasing matrix of positive singular values. We can then compute the pseudo-inverse of  $\mathbf{C}_x$  :

$$\mathbf{C}_x^\dagger = \mathbf{V}_x \mathbf{\Delta}_x^\dagger \mathbf{U}_x^H \quad (10)$$

where each term of the diagonal matrix  $\Delta_x^\dagger$  is the inverse of corresponding term in  $\Delta_x$  except for nul values. Once  $C_x$  and  $C_x^\dagger$  are computed, phase estimation can be performed by :

$$\widehat{\mathbf{a}}_2 = arg(\gamma_{x,estim}) \quad (11)$$

where  $\widehat{\mathbf{a}}_2$  is the estimated tip coefficient vector, and  $\gamma_{x,estim} = C_x^\dagger T_x$ . Here, we retrieve the global tip as expected. Eq.(11) is well suited to a real-time system since  $C_x^\dagger$ , which only depends on the instrumental setup, can be pre-computed once for all. The same operations are performed for the other direction.

This algorithm can be used to align the sub-apertures, in open loop if absolute calibration is sufficient or in close-loop otherwise. In this case, the non-overlapping hypothesis is no longer valid at the end. To solve for this, an extension of this algorithm has been derived.<sup>11</sup> In the next section, we present global results of the coarse alignment using ELASTIC algorithm plus its refinement.

### 2.3 Performance evaluation

We present in this section the sensor response to a tip-tilt error. The following simulations were performed with the seven subaperture configuration as shown in Fig.2. The object is an unresolved source and the quasi-monochromatic images of size 256x256 pixels are simulated with photon noise, a 10 electrons per pixel read-out-noise with a maximum value of 1000 photon per pixel. They are sampled at the Shannon rate.

Fig.3 shows the estimation bias regarding the tip-tilt perturbation. The amplitude of the perturbations was chosen from 0 to 25 rad RMS, corresponding to the image boundaries (with more than 25 rad RMS, the spot is out of the field). We can see that the algorithm bias is less than 0.2 rad RMS in 20% of the cases, and less than 2 to 4 rad RMS in 100% of the cases. More important, the estimation bias decreases with the perturbation amplitude. Indeed, the bias is less than 0.2 rad RMS for 100% of the cases when the perturbation amplitude becomes lower than 1 rad RMS.

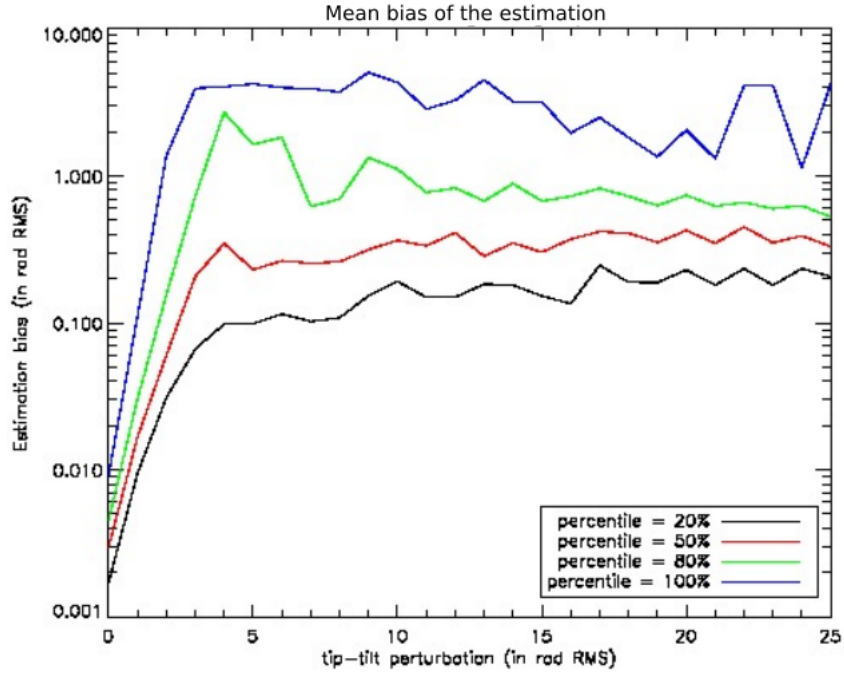


Figure 3. Estimation bias regarding the amplitude perturbation. The graph shows the distribution of the bias over 100 random outcomes of tip-tilt aberrations in a HEXA7 pupil configuration. Photometry used in this example was: Maximum of the image at 1000 photo-electrons and a 10 electrons RON.

We can thus claim that the system can be brought in a less than 0.2 rad RMS amplitude tip-tilt perturbation, by using ELASTIC in a closed loop. As we will see in the following sections, it corresponds to the input range of the small amplitude error estimation algorithm.

## 2.4 Experimental results

### 2.4.1 A dedicated bench for multiple-aperture cophasing

In order to test and validate the algorithm, we have a dedicated experimental bench.<sup>12</sup> Figure 5 illustrates the optical bench, the following paragraphs will present different important parts of the bench : the source module, the multiple-aperture mirror and the detection module.

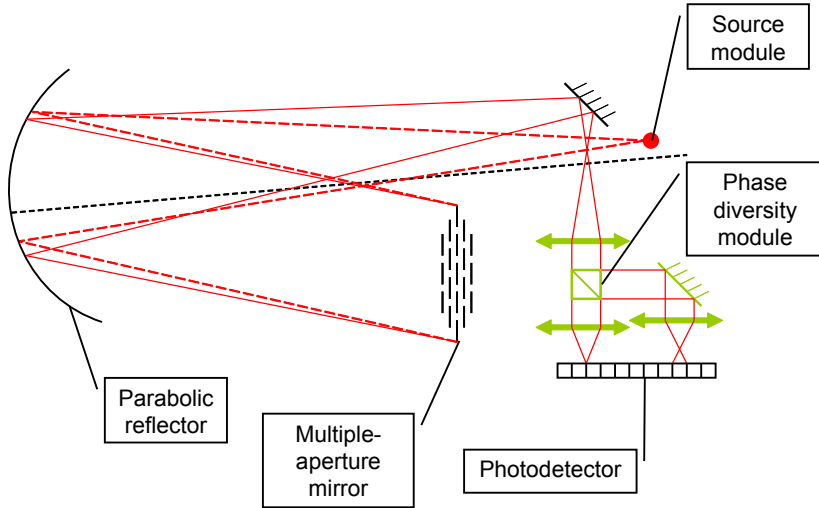


Figure 5. Multi-aperture mirror, manufactured by GEPI

Figure 4. Scheme of the optical bench used for the experimental validation of the sensor.<sup>13</sup>

**The source module** We can select 2 different types of source. A Thorlabs fibered laser diode emitting at 635 nm is used as an unresolved source. The other is an Oled device, emitting at 550 nm, with a resolution of 852x600 pixels, used as a resolved source.

**The multiple-aperture mirror** This module is a multiple-aperture mirror manufactured by GEPI (Galaxies, Etoiles, Physique et Instrumentation) laboratory of Observatoire de Paris. As we can see on Figure 6, it is composed by nineteen mirrors. In order to introduce perturbations in the pupil plane, each mirror is held by three piezoelectric components. These have no control loop and they suffer from hysteresis. Thus each displacement is not perfectly deterministic.

**The detection module** As we can see on Figure 5, the detection module is used to obtain the two images on the detector. A first lens collimates the diverging incoming beam, then a cube splits the beam in two, and the two other lenses refocus the image on two different areas of the camera. One is at the focal distance of the lense, the other can be translated to choose the desired defocus.

### 2.4.2 Loop closure on an unresolved source

To validate the algorithm, we succeeded in aligning a strongly misaligned multi-aperture instrument. We present the alignment of a HEXA 7 pupil configuration, as we can see Fig.2 and Fig.5 (center part of the mirror), on an unresolved object. Unfortunately, the phase-diversity sensor was not designed with the requirement of large-amplitude diversity required by the ELASTIC algorithm. We thus replaced the spatial diversity by a temporal diversity, applying on each segment tip/tilt offsets similar to thoses that the global defocus would have introduced.

As we can see Fig.6, we managed to align the instrument from a large amplitude to a small amplitude error case (where the small-amplitude algorithm can then take over and perform the fine corrections). The introduced

gain of the loop closure has been on purpose chosen low (gain = 0.05) in order to have a precised control over each sub-aperture. This alignment test took less than a minute. We are currently working on an optimization to reduce this duration. We can notice fringes when two spots are close or superimposed. They are due to the interferences between two sub-apertures and occur even without piston correction because of the long coherence length of the source.

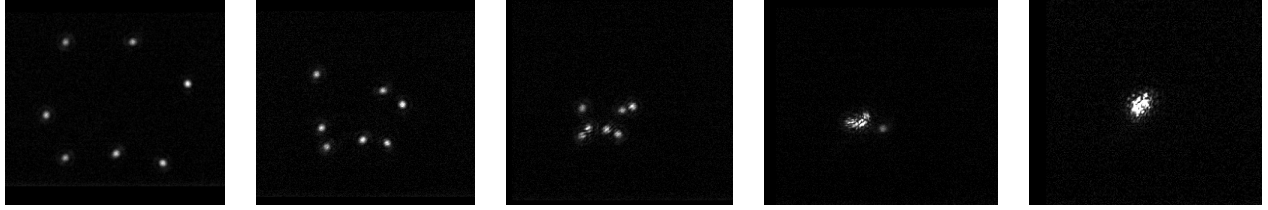


Figure 6. Loop closure with the ELASTIC algorithm estimating tip/tilt aberrations. Iterations are 0, 10, 20, 25 and 30. We only show here the focal image.

### 3. SMALL AMPLITUDE PISTON-TIP-TILT ALIGNMENT BY PHASE DIVERSITY

Phase Diversity is now routinely used for the calibration of optical instruments, and is particularly suited for the calibration of multi-aperture instruments. However, the corresponding algorithms are most often time-consuming.

However, when residual aberrations are in a small range, as it is the case after the ELASTIC algorithm alignment, quick, linearized algorithms can be used. We therefore followed Mocoer's<sup>7</sup> approach to write the LAPD (Linearized Analytical Phase Diversity) algorithm, which allows a precise piston and tip-tilt measurement over about one radian range.

#### 3.1 The LAPD Algorithm

The algorithm supposes that the perturbations are small enough to allow a 1<sup>rst</sup> order Taylor developpment of the PSF  $\mathbf{h}$  versus the aberration vector  $\mathbf{a}$  (Eq.12):

$$\mathbf{h}(\mathbf{a}) = \mathbf{h}(\mathbf{0}) + \mathbf{a} \cdot \mathbf{grad}(\mathbf{h}) + o(\mathbf{a}) \quad (12)$$

where  $\mathbf{a} = (a_{0,0}, a_{0,1}, \dots, a_{k,n}, \dots)$  is the vector of the Zernike coefficients of the residual perturbations we want to measure,  $k$  the Zernike mode,  $n$  the index of the sub-aperture, and  $\mathbf{grad}(\mathbf{h}) = \left( \frac{\partial \mathbf{h}}{\partial a_{0,0}}, \frac{\partial \mathbf{h}}{\partial a_{0,1}}, \dots, \frac{\partial \mathbf{h}}{\partial a_{k,n}}, \dots \right)$  the  $(k, n)$  Jacobian matrix of  $\mathbf{h}$ .

Doing so, Mocoer showed that the Phase Diversity criterion of two images  $\tilde{\mathbf{i}}_1$  and  $\tilde{\mathbf{i}}_2$  whose PSFs are  $\mathbf{h}_1$  and  $\mathbf{h}_2$  could be simply written :

$$J(\mathbf{a}) = \frac{1}{2\sigma^2} \sum_{\nu} |\mathbf{A}(\nu)\mathbf{a} - \mathbf{B}(\nu)|^2 + \text{Cst} \quad (13)$$

where

$$\begin{aligned} \mathbf{A}(\nu) &= \frac{1}{\mathbf{C}(\nu)} [\tilde{\mathbf{i}}_2(\nu)\boldsymbol{\alpha}_1(\nu) - \tilde{\mathbf{i}}_1(\nu)\boldsymbol{\alpha}_2(\nu)] \\ \mathbf{B}(\nu) &= \frac{1}{\mathbf{C}(\nu)} [\tilde{\mathbf{i}}_1\boldsymbol{\beta}_2(\nu) - \tilde{\mathbf{i}}_2(\nu)\boldsymbol{\beta}_1(\nu)] \\ \mathbf{C}(\nu) &= \sqrt{|\boldsymbol{\beta}_1(\nu)|^2 + |\boldsymbol{\beta}_2(\nu)|^2 + \epsilon} \end{aligned} \quad (14)$$

and

$$\begin{aligned}\boldsymbol{\alpha}_{1,2} &= FT[\mathbf{grad}(\mathbf{h}_{1,2}(\mathbf{a} = \mathbf{0}))] \\ \boldsymbol{\beta}_{1,2} &= FT[\mathbf{h}_{1,2}(\mathbf{a} = \mathbf{0})]\end{aligned}\tag{15}$$

$\mathbf{A}$ ,  $\mathbf{B}$  and  $\mathbf{C}$  are matrices that can be easily computed from the image formation model.

Then  $\mathbf{a}$  can be estimated analytically by a simple matrix inversion because  $J(\mathbf{a})$  in Eq. 13 is quadratic in  $\mathbf{a}$ :

$$\hat{\mathbf{a}} = [\Re(\mathbf{A}^H \mathbf{A})]^\dagger \cdot [\Re(\mathbf{A}^H \mathbf{B})]\tag{16}$$

### 3.2 Numerical experiments

Numerical experiments were performed on a very wide set of random tip-tilt-piston aberrations, in several configurations including realistic noise, in order to estimate the accuracy and the range of the LAPD algorithm. An example of result is shown on Fig.7 :

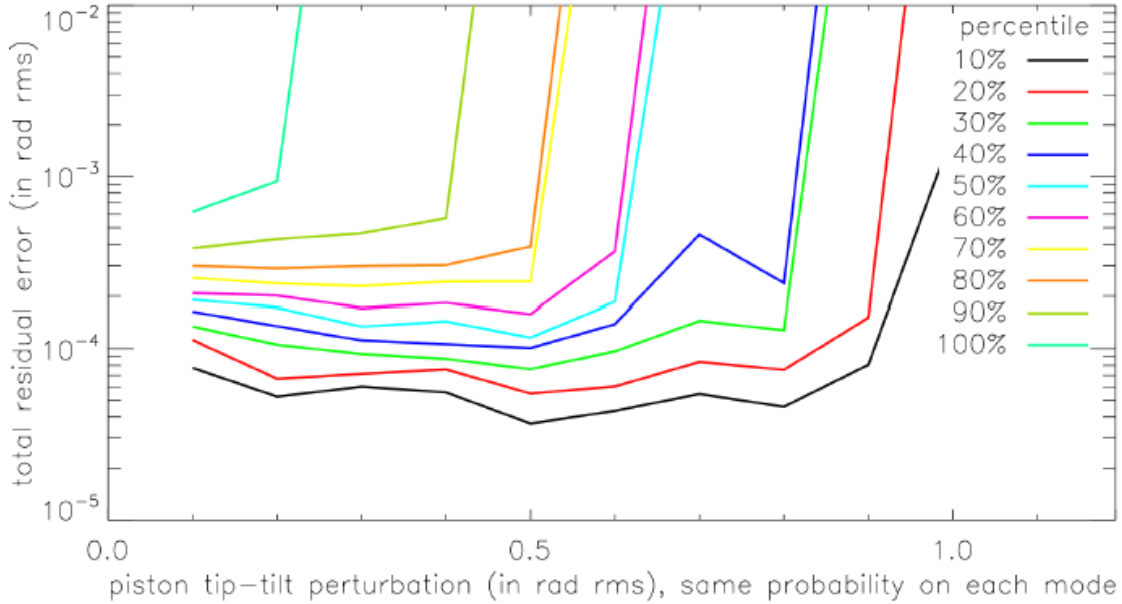


Figure 7. Example of simulation results, showing the distribution of the errors over 1000 random trials of piston tip-tilt aberrations in a 3-apertures configuration. Similar results were obtained with more subapertures. NB : the photometry used in this example was: maximum of the image at 20000 photo-electrons and a 10 electron RON.

The results are very promising :

- better than 0.01 rad rms to 0.05 rad rms accuracy (depending on the number of the subapertures) is obtained in 100 % of the cases over a 0.35 rad rms perturbation, and in more than 50 % of the cases over a 1 rad rms perturbation.
- if tip-tilt perturbations are limited to 0.1 rad rms, which is a reasonable assumption, then the same accuracy is obtained in 100 % of the cases over a larger than 1 rad rms piston range.
- less than 0.3 seconds, with IDL and an average laptop, where needed in order to compute pistons in a 19 aperture configuration.

Now these results have to be confirmed by experimentations on the BRISE test bench.

## 4. CONCLUSION

We introduced a new algorithm, ELASTIC, based on a "geometric diversity" of larger amplitude and a simple and non-supervised algorithm, to perform the initial step of large amplitude tip-tilt error estimation. As experimentally demonstrated, this algorithm can bring a strongly misaligned segmented instrument in a coarsely aligned state. Then a large amplitude piston alignment can be operated (by a simple 1D scan of the segments, with active tip/tilt control by ELASTIC) until all conditions are met to start the fine phasing. We then have demonstrated here that a linearized fast version can be used on a 3 or more sub-aperture pupil.

This procedure has an impact on the hardware : indeed the diversity amplitude needs to be relatively large for the initial alignment, and relatively small for the fine phasing. The solution we demonstrated on our bench is to use a fixed spatial diversity for the fine phasing during observation and a temporal modulation (a "pseudo-defocus" obtained by applying best-fit piston/tip/tilt on the segments themselves) for the large diversity required by ELASTIC during the initial alignment. Therefore, ELASTIC can be implemented without any additional hardware.

Our short-term perspective is to confirm the LAPD algorithm simulation results by experimentations on the BRISE test bench. We then aim at extending ELASTIC to the case of extended objects.

## REFERENCES

- [1] Sauvage, M. et al., "A development roadmap for critical technologies needed for talc: a deployable 20m annular space telescope," *Proc. SPIE* (9904-51) (2016).
- [2] Spergel, D. et al., "Wide-Field InfraRed Survey Telescope-Astrophysics Focused Telescope Assets WFIRST-AFTA Final Report," *ArXiv e-prints* (May 2013).
- [3] Mesrine, M., Thomas, E., Garin, S., Blanc, P., Alis, C., Cassaing, F., and Laubier, D., "High resolution Earth observation from geostationary orbit by optical aperture synthesis," in [*Sixth International Conference on Space Optics*], ESA-CNES (June 2006).
- [4] Baron, F., Mocoëur, I., Cassaing, F., and Mugnier, L. M., "Unambiguous phase retrieval as a cophasing sensor for phased array telescopes," *J. Opt. Soc. Am. A* **25**, 1000–1015 (May 2008).
- [5] Gonsalves, R. A., "Phase retrieval and diversity in adaptive optics," *Optical Engineering* **21**(5), 215829–215829– (1982).
- [6] Mugnier, L. M., Blanc, A., and Idier, J., "Phase diversity: a technique for wave-front sensing and for diffraction-limited imaging," *Advances in Imaging and Electron Physics* **141**, 1–76 (2006).
- [7] Mocoëur, I., Mugnier, L. M., and Cassaing, F., "Analytical solution to the phase-diversity problem for real-time wavefront sensing," *Optics letters* **34**(22), 3487–3489 (2009).
- [8] Thurman, S. T., "Method of obtaining wavefront slope data from through-focus point spread function measurements," *J. Opt. Soc. Am. A* **28**, 1–7 (Jan 2011).
- [9] Jurling, A. S. and Fienup, J. R., "Extended capture range for focus-diverse phase retrieval in segmented aperture systems using geometrical optics," *J. Opt. Soc. Am. A* **31**, 661–666 (Mar 2014).
- [10] Carlisle, R. E. and Acton, D. S., "Demonstration of extended capture range for james webb space telescope phase retrieval," *Appl. Opt.* **54**, 6454–6460 (Jul 2015).
- [11] Cassaing, F. and Vievard, S., "Large amplitude fast estimation of tip/tilt for multiple-aperture systems by geometric diversity," *to be submitted* (2016).
- [12] Cassaing, F., Sorrente, B., Mugnier, L., Rousset, G., Michau, V., Mocoëur, I., and Baron, F., "Brise: a multipurpose bench for cophasing sensors," in [*Advances in stellar interferometry*], Monnier, J. D. and Schöller, M., eds., **6268** (2006).
- [13] Denolle, B., Cassaing, F., Montri, J., Lisowski, J., and Amans, J. P., "Real-time focal-plane wavefront sensing for compact imaging phased-array telescopes: numerical and experimental demonstration," *Proc. SPIE* **8713**, 87130J–87130J–10 (2013).